

ORIGINAL ARTICLE OPEN ACCESS

Cretaceous Chert-Hosted Microfossils Visualized With Synchrotron Ptychographic X-Ray Computed Tomography (PXCT)

Kelsey R. Moore^{1,2}  | Theodore M. Present¹  | Antoine Crémière^{1,3} | Manuel Guizar-Sicairos^{4,5}  | Mirko Holler⁴ | Andrew Barnett⁶ | Kristin Bergmann⁷ | Joachim Amthor^{8,9} | John Grotzinger¹

¹Division of Geological and Planetary Sciences, California Institute of Technology, Pasadena, California, USA | ²Department of Earth and Planetary Sciences, Johns Hopkins University, Baltimore, Maryland, USA | ³Geo-Ocean UMR 6538 CNRS-Ifremer-UBO-UBS, Plouzane, France | ⁴Photon Science Division, Paul Scherrer Institute, Villigen, Switzerland | ⁵École Polytechnique Fédérale de Lausanne (EPFL), Institute of Physics, Lausanne, Switzerland | ⁶Shell UK, London, UK | ⁷Department of Earth, Atmospheric and Planetary Sciences, Massachusetts Institute of Technology, Cambridge, Massachusetts, USA | ⁸Shell Brazil Petróleo, Rio de Janeiro, Brazil | ⁹Division of Earth Sciences and Geography, Rhine-Westphalia Technical University of Aachen, Aachen, Germany

Correspondence: Kelsey R. Moore (kmoor101@jh.edu)

Received: 17 January 2025 | **Revised:** 10 April 2025 | **Accepted:** 12 April 2025

Funding: Funding for this project was provided by the Simons Foundation through a grant to JPG and the Paul Scherrer Institute Swiss Light Source.

Keywords: Barra Velha Formation | chert | microfossil | pre-salt | ptychographic X-ray computed tomography

ABSTRACT

Silicification of microfossils is an important taphonomic process that provides a record of microbial life across a range of environments throughout Earth history. However, questions remain regarding the mechanism(s) by which silica precipitated and preserved delicate organic material and detailed cellular morphologies. Constraining the different mechanisms of silica precipitation and identifying the common factors that allow for microfossil preservation is the key to understanding ancient microbial communities and fossil-preserving mechanisms. Here, we use synchrotron ptychographic X-ray computed tomography (PXCT) as a novel technique to analyze microfossils from the Cretaceous Barra Velha Formation and better characterize their diverse morphologies and preservation styles. Through this technique, we generate 2D and 3D reconstructions that illustrate the microfossils and silica-organic textures at nanometer resolution. At this resolution, we identify previously uncharacterized silica textures and organic-silica relationships that help us relate findings from modern silicifying environments and experimental work to the fossil record. Additionally, we identify primary morphological differences among the microfossils as well as preservational variability that may have been driven by physiological and/or biochemical differences between the different organisms that inhabited the Cretaceous pre-salt basin. These findings help us to better characterize the diversity and complexity of the microbiota in this ancient basin as well as taphonomic processes and biases that may have driven microfossil preservation in this and other silicifying environments throughout Earth history.

1 | Introduction

Early diagenetic or primary chert deposited in shallow environments preserves an important record of the microbial biosphere

throughout Earth's history. In addition to preserving kerogen and microbial textures, this chert sometimes preserves body fossils of the microbial cells, providing a window into the morphologies of the microbes and the complexity and diversity of the

Kelsey R. Moore and Theodore M. Present are co-first authors.

This is an open access article under the terms of the [Creative Commons Attribution-NonCommercial-NoDerivs](https://creativecommons.org/licenses/by-nc-nd/4.0/) License, which permits use and distribution in any medium, provided the original work is properly cited, the use is non-commercial and no modifications or adaptations are made.

© 2025 The Author(s). *Geobiology* published by John Wiley & Sons Ltd.

communities. This exceptional taphonomic window is thought to be the result of rapid precipitation of silica from fluids at or near the sediment–water interface, allowing for the rapid entombment of the delicate microbial cells and organic matter before they can be degraded. However, the specific mechanisms of chert precipitation, the amorphous or crystalline nature of the initial silica phases, their associations with organic matter, and the taphonomic biases that accompany preservation by chert are poorly understood and in need of further study.

The different possible mechanisms of silicification and taphonomic trends have been studied through petrographic analyses of ancient fossiliferous chert (Knoll et al. 2013; Manning-Berg and Kah 2017; Manning-Berg et al. 2018, 2019; Nabhan et al. 2021), studies of modern silicifying environments (Walter et al. 1972; Ferris et al. 1986; Schultze-Lam et al. 1995; Jones and Renaut 1996; Konhauser and Ferris 1996; Jones et al. 1997, 1998, 2001, 2004, 2005; Konhauser et al. 2001; Campbell et al. 2002, 2015; Cady and Farmer 1996; Aubrecht et al. 2008; Sauro et al. 2018; Slagter et al. 2019; Gong et al. 2020; Suchý et al. 2021; Wilmeth et al. 2021), and experimental work that allowed for direct observation of silica precipitation and cell preservation (Francis, Barghoorn, et al. 1978; Francis, Margulis, et al. 1978; Urrutia and Beveridge 1993, 1994; Westall 1995; Phoenix et al. 2000; Toporski et al. 2002; Yee et al. 2003; Benning et al. 2004; Lalonde et al. 2005; Orange et al. 2009; Moore et al. 2020, 2021; Slagter et al. 2021, 2022). Together, these studies have revealed multiple mechanisms by which silicification may occur under a range of conditions with different concentrations of silica, temperatures, pH, alkalinity, and salinity. Additionally, these collective studies have highlighted the potential for silicification to be either abiotically driven (e.g., Konhauser et al. 2001; Oehler 1976) or microbially influenced (e.g., Benning et al. 2004; Ferris et al. 1988, 1986; Jones and Renaut 2003; Moore et al. 2021, 2020; Orange et al. 2009), depending on the conditions and the microbial communities present.

Although multiple different mechanisms may explain the preservation of microbial body fossils in various environments throughout Earth's history, these mechanisms—whether abiotically driven or microbially influenced—share some important features. Both environmental studies and laboratory experiments have revealed that the initial silica phases that tend to form in association with microbial cells are amorphous to nanocrystalline, typically characterized by colloidal silica particles (Walter et al. 1972; Ferris et al. 1986; Schultze-Lam et al. 1995; Jones and Renaut 1996; Konhauser and Ferris 1996; Jones et al. 1997, 1998, 2001, 2004, 2005; Konhauser and Urrutia 1999; Konhauser et al. 2001; Campbell et al. 2002, 2015; Cady and Farmer 1996; Gong et al. 2020; Moore et al. 2020, 2021; Wilmeth et al. 2021). Additionally, many of these studies suggest that the nucleation point for the silica under both saturated (Francis, Barghoorn, et al. 1978; Francis, Margulis, et al. 1978; Westall 1995; Toporski et al. 2002; Benning et al. 2004; Orange et al. 2009; Slagter et al. 2021, 2022) and undersaturated (Urrutia and Beveridge 1993, 1994; Moore et al. 2020, 2021) conditions is the exopolymeric substances (EPS) around the cells, a key factor that relates to the preservation of the EPS and cells. Indeed, some studies even suggest that certain organic compounds and microbes may more readily nucleate silica than others (Francis, Barghoorn, et al. 1978; Francis, Margulis, et al. 1978; Urrutia and Beveridge 1993, 1994; Westall 1995; Phoenix et al. 2000; Yee et al. 2003; Lalonde et al. 2005; Orange et al. 2009; Moore

et al. 2020, 2021). If true, this would suggest certain taphonomic biases in the chert-hosted microbial fossil record as well as some key organic-silica interactions that facilitate the initial stages of silica nucleation and organic preservation. However, further characterization of chert-hosted microfossils and organic matter is needed in order to fully assess the relevance of these mechanisms for ancient environments and their implications for the past microbial communities.

Chert from the Cretaceous Barra Velha Formation (Santos Basin, offshore southeastern Brazil) provides an opportunity to assess these key components—nanocrystalline to amorphous silica phases and silica-EPS interactions—as well as nuanced differences in organism-specific silicification in the rock record. The Barra Velha Formation is one of the Cretaceous “pre-salt” deposits, a group of deposits that formed in the pre-Atlantic rift basin during the rifting of Gondwana (Moreira et al. 2007; Carminatti et al. 2008; Nakano et al. 2009). Rare authigenic chert from the Barra Velha Formation is thought to have precipitated rapidly from saturated fluids that were introduced sporadically into this ancient, alkaline lake (Moore et al. 2024). As a result, the chert preserved a range of microfossil morphotypes that likely represent a diverse community of bacteria and simple eukaryotes that inhabited the ancient rift basin. Though chert precipitation was likely abiotic, the style and degree of preservation of the different microfossils point to potential taphonomic differences across different organisms. These taphonomic differences are an important component of our understanding of the pre-salt basin and other ancient environments broadly because they may relate to differences in organic-silica interactions that drive silica nucleation and organic preservation across complex communities.

Here, we utilize ptychographic X-ray computed tomography (PXCT) as a novel method to analyze microfossils preserved in chert from the Cretaceous Barra Velha Formation (Figure 1) and better characterize the organic textures and the silica-organic associations. We identify key chemical and textural features that relate the style of preservation of the ancient microfossils to findings from modern environmental and experimental work. In particular, we compare these textures and relationships to studies that point to the importance of EPS-silica interactions in silica nucleation and organic preservation as well as the importance of nanocrystalline to amorphous phases in microfossil preservation. Through this technique, we characterize the kerogen and microfossils in three-dimensions (3D) at nanometer resolution and identify the differences and similarities in the degree and nature of organic preservation across fossil morphotypes. Through this work, we gain a better understanding of the mechanisms of silicification in ancient environments as well as the role of organic-silica interactions in fossil preservation. Additionally, we identify possible differences in the preservation potential of different organisms that may relate to cell physiology even under conditions that allow for abiotic silica precipitation.

2 | Geologic Setting

The Aptian Barra Velha Formation is one of the “pre-salt” deposits that together record the Cretaceous rifting of Gondwana (Moreira et al. 2007; Carminatti et al. 2008; Nakano et al. 2009). The Barra Velha Formation was deposited during the post-rift to

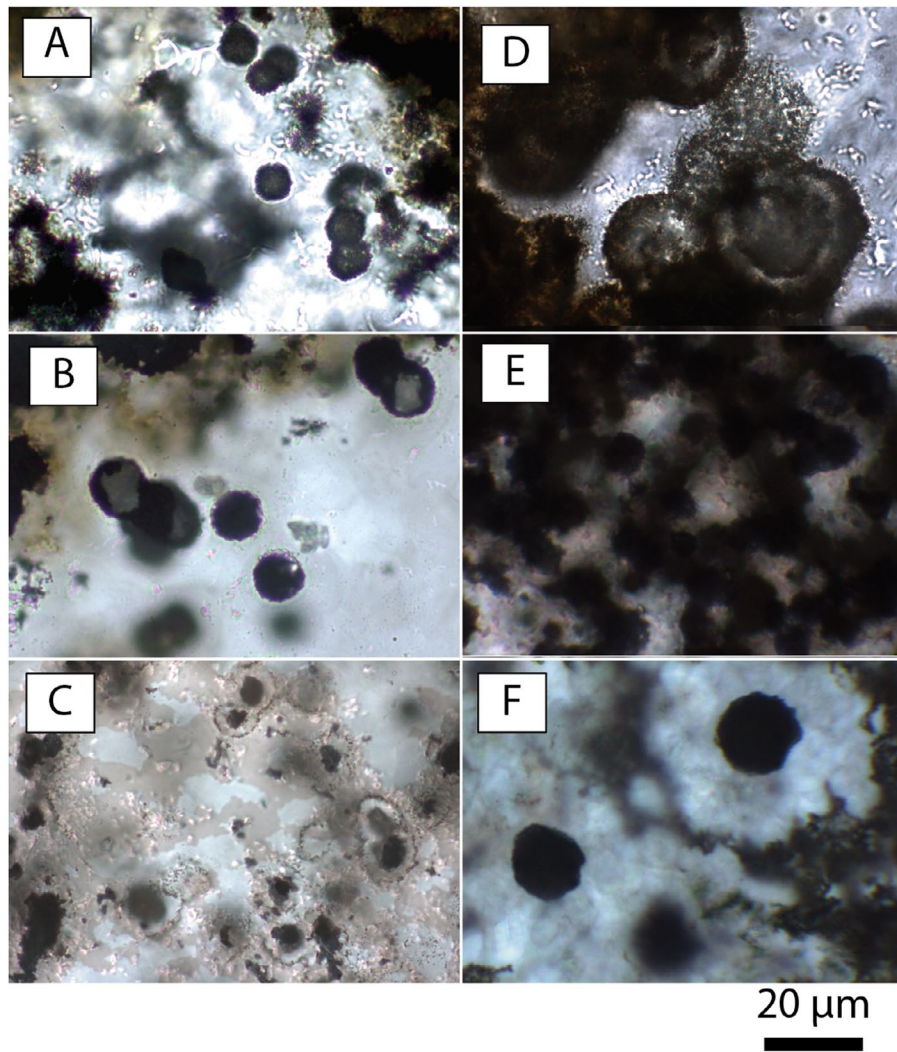


FIGURE 1 | Transmitted light photomicrographs of the six microfossil morphotypes analyzed in this study and previously described in Moore et al. 2024 (A = 1, B = 2, C = 4, D = 7, E = 10, F = 11). Transmitted light images allow for a direct comparison of the morphological and textural features visible through classic petrographic techniques alongside those visible in axial tomographic slices (Figures 2 and 4) and 3D renderings (Figure 6).

sag phase of rifting in the proto-Atlantic basin. Previous studies of the Barra Velha Formation and other pre-salt deposits have suggested, based on mineralogical and geochemical data, that the proto-Atlantic basin was a series of massive alkaline lakes (Wright 2020). While the majority of the pre-salt deposits are dominated by carbonate facies, including the enigmatic and well-studied carbonate spherulite and shrub facies and associated Mg-silicate clays (Wright 2012; Wright and Barnett 2015; Pietzsch et al. 2018, 2020; Mercedes-Martín et al. 2019; Carramal et al. 2022), the Barra Velha Formation also contains rare, microfossiliferous chert among the carbonate facies (Moore et al. 2024). Recent studies investigated these chert-rich facies and interpreted that the microfossiliferous chert represented a syndimentary, authigenic silica that precipitated as a result of changing water chemistry in the basin after the formation of the carbonates and dissolution due to karstification (Moore et al. 2024; Wood et al. 2024). The microfossils preserved in the chert (Figure 1) represent a unique window into the microbiota that inhabited either the karsted environments in the basin, newly introduced river-water, or a combination of these. However, the diversity and preservation mechanisms of the

microfossils remain in question. The samples analyzed in this study come from two samples of microfossiliferous chert from drill cores of the Barra Velha Formation. The samples were extracted from drill cores from a well c. 20 km to the north of the Iracema Field. They were taken at 39.5 m (sample S4) and 71 m (sample S8) below the base of salt in an interval immediately underlying the informally named “Lula’s Fingers” (cf. Wood et al. 2024). Unlike the carbonate facies typically described from the pre-salt deposits, these samples are from rare microfossiliferous chert boundstone facies that contain carbonate intraclasts as well as organic matter, microbial textures, and microfossils.

3 | Methods

3.1 | Sample Preparation

Two microfossiliferous samples of the Barra Velha Formation were prepared as round, 1-in. diameter, 100 μm thick sections by Wagner Petrographic. Each of the two thick section rounds was imaged and mapped using scanning electron microscopy (SEM)

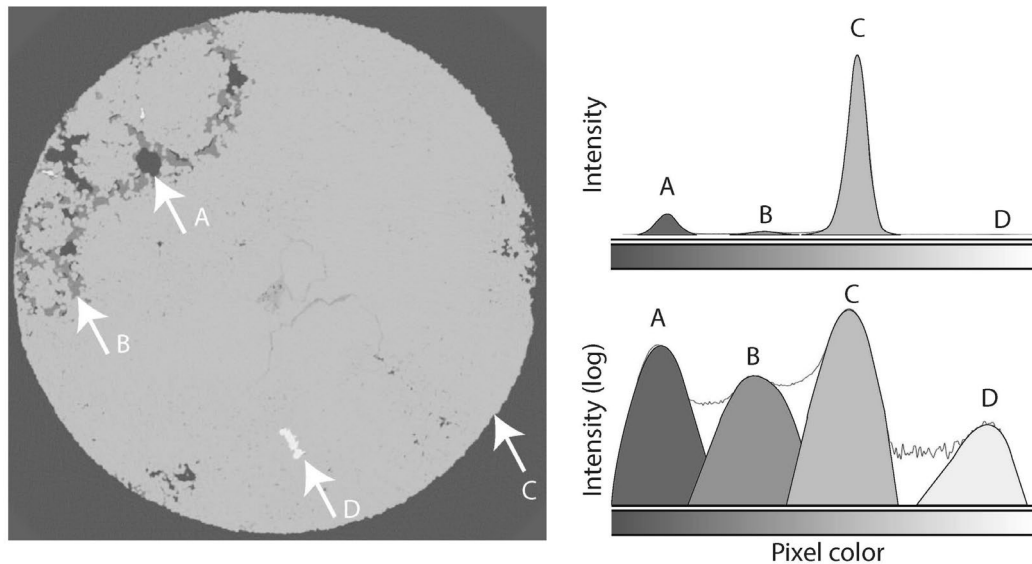


FIGURE 2 | Example 2D axial tomographic slice (left) and corresponding pixel intensity histograms with normal (top right) and log (bottom right) scale intensity from sample S4. The axial tomographic slice and corresponding pixel intensity histograms illustrate the major and minor material classes which are distinguished by their pixel intensity and related electron density and material density. Material classes include void space (A: Dark grey), kerogen (B: Mid-tone grey), chert (C: Light grey) and rare high density material (D: Lightest grey/white). The axial tomographic slice highlights the chert matrix and the circular wall shapes composed of kerogen and void space preserved in the chert.

and transmitted and reflected light microscopy. Uncoated thick sections were mapped on a Hitachi SU3500 variable pressure scanning electron microscope (VP-SEM) with an Oxford Instruments X-Max^N 150 mm² silicon drift energy dispersive spectroscopy (EDS) system. Samples were mapped under 30 Pa pressure at 15 keV with a 10 mm working distance at a magnification of 150 \times using the mosaic mode with AZtec software (Oxford Instruments) to generate a mosaic BSE map of each entire 1-in. diameter thick section round. Thick section rounds were then mapped using a Leica DM6000B microscope with a motorized stage and Leica Application Suite (LAS) software at 20 \times magnification to generate full area mosaic transmitted and reflected light maps of each thick section.

Regions of interest were identified using all three full area maps of each sample based on the abundance and diversity of microfossils present within a 60 μ m diameter circle. Two 60 μ m diameter and 60 μ m tall FIB-milled cylinders were prepared from each sample at the Scientific Center for Optical Microscopy (ScopeM) facility at ETH Zurich. Cylinders were prepared using a carbon target on a Helios 5UX FIB-SEM and mounted onto OMNY tomographic pins (Holler et al. 2017; Maldanis et al. 2020) to be analyzed using PXCT (Dierolf et al. 2010; Holler et al. 2017).

3.2 | PXCT Analysis

The mounted, FIB-milled cylinders were analyzed by PXCT on the coherent small-angle X-ray scattering (cSAXS) beamline at the Swiss Light Source (SLS), Paul Scherrer Institute, Switzerland, over the course of two beam time sessions. In the first session, two samples (S4_1 and S8_1) were analyzed using the FLOMNI setup (Holler et al. 2012, 2017; Maldanis et al. 2020) with a photon energy of 6.2 keV. The beam was focused using a Fresnel zone plate of 60 nm outermost zone width and 200 μ m

diameter, which is illuminated coherently by using a slit with a horizontal opening of 20 μ m, which functions as a secondary source. The lens is fabricated with engineered wavefront distortions that improve the quality and resolution of the ptychography reconstructions (Odstrčil, Lebugle, et al. 2019). The sample was located 1.6 mm downstream of the focus where the beam diameter is 5.3 μ m. Scans were conducted with a field of view of 80 μ m \times 83 μ m for sample S4_1 and 80 μ m \times 45 μ m for sample S8_1 with a step size of 2.5 μ m and following a Fermat spiral pattern (Huang et al. 2014). At each point of the scan, a far-field diffraction pattern was measured using an in-vacuum Eiger 1.5 M detector (Guizar-Sicairos et al. 2014) located 5 mm downstream from the sample with an exposure time of 0.05 s for both samples. Ptychographic reconstructions were carried out using the PtychoShelves package (Wakonig et al. 2020) with 1000 iterations of the difference map (Thibault and Guizar-Sicairos 2012) followed by 500 iterations of refinement using maximum likelihood (Thibault and Guizar-Sicairos 2012). For the reconstructions, 400 \times 400 pixels of the detector were utilized, yielding a pixel size of 39.71 nm. A total of 640 ptychographic projections were measured for each sample. The angular distribution in sample S4_1 followed a nested binary acquisition with base 8 (Kaestner et al. 2011) which allows for obtaining the data in portions of faster intermediate overviews during the acquisition; those intermediate overviews allow verifying that there is no radiation damage, and upon combination provide a fully angularly sampled set of tomographic projections that is then used to compute the tomogram at the best resolution using all the data. The projections of sample S8_1 were acquired equally spaced with an angular spacing of 8 $^\circ$, and the starting angles were following a golden ratio distribution. Tomographic projections were unwrapped and a linear phase component removed (Guizar-Sicairos et al. 2011) before an iterative algorithm based on tomographic consistency was used to align them to sub-pixel precision (Odstrčil, Holler, et al. 2019). Resolution was estimated

by the intersection of the Fourier shell correlation (FSC) curve with the $\frac{1}{2}$ -bit threshold (van Heel and Schatz 2005). Resulting half-pitch resolutions were 164.28 nm for S4_1 and 120.20 nm for S8_1. In the second session, samples S4_2 and S8_2 were analyzed using similar parameters except with a detector distance to the sample of 5.23 m and a resulting pixel size of 35 nm.

3.3 | Data Processing

PXCT analyses yielded 2D axial tomographic slices of all four samples. 3D renderings were generated using Matlab. In addition to the visualization of the 3D structures of the microfossils, data were analyzed using ImageJ to characterize the materials and the textural and morphological characteristics of the microfossils and the surrounding chert. Representative axial tomographic slices were selected from each of the four data sets to encompass each of the different microfossil morphotypes preserved across the samples. Within each axial tomographic slice and full 3D rendering, the gray values provide the local quantitative electron density (Diaz et al. 2015) which can be used to determine material density and material identity. Using both ImageJ and Matlab, histograms were generated for axial tomographic slices and full tomograms, which showed three main peaks and one additional peak that appears rarely in some regions of the samples. These peaks correspond to the dominant “material classes” that are present in the samples.

To fit the distribution of electron densities using Matlab, the data were randomly subsampled to 1 million data points, and electron densities lower than $0.2 e^-/\text{\AA}^3$, representing pore space, were excluded. A Gaussian Mixture Model (GMM) was fit to the distribution of the subsampled, pore-excluded electron density data with a convergence tolerance of -6 on the log-likelihood function. Three components were used in fitting, as voxels that were nanoscale mixtures of materials cannot be fit by a sum of gaussian distributions (Pedersen et al. 2015). An additional high-density phase was observed in sample S4_2 and fit with an additional component (Video S1–S5), and two components were needed to fit the largest (quartz) peak in that sample as well. Three-dimensional visualizations of the kerogen component were generated using Matlab's Image Processing Toolbox from the Gaussian component corresponding to the kerogen phase. The electron density volume was displayed with a transparency map set using a piecewise linear function of the electron density in which the kerogen was rendered opaque at the kerogen component's mean density, and alpha values decreased linearly to a small value one standard deviation above and below the mean. Above one standard deviation, the alpha was set to the small value, making denser chert voxels translucent and white, and below one standard deviation, voxels representing pore spaces were transparent.

Using electron densities, material densities were calculated for each of the materials using the formula $\rho = n_e A / (N_A Z)$ where ρ is the material density, n_e is the electron density, N_A is Avogadro's number, and A and Z are the molar mass and number of electrons, respectively, of a given material. Based on previous work that identified both chert and kerogen in these materials (Moore et al. 2024), we assumed values for quartz and organic material with A/Z of 2 and $1.92 \text{ g/mol}/e^-$, respectively.

4 | Results

4.1 | Density and Classification of Materials

The 2D axial tomographic slices and 3D renderings from all samples analyzed revealed three dominant components in the samples (Figure 2A–C) and one additional minor component that corresponds to a rare high-density material (Figure 2D). These materials are distinguishable based on shades of grey that comprise the samples—dark (Figure 2A), mid-tone (Figure 2B), and light gray (Figure 2C)—where the shade of the voxels correlates to the electron density of the material. Histograms and Gaussian fits generated from the 3D renderings reveal minor variability in the peak centers (Figure 3), but the density distributions overlap. Colorized versions of representative axial tomographic slices highlight the three dominant components as teal, purple, and orange (Figure 4). The matrix of the cylinders is composed of material represented by the light grey or orange regions and is surrounded by a dark grey or teal region. This darkest grey or teal corresponds to void space and is, therefore, essentially an absence of mass and provides a baseline of zero electron density. The mid-tone grey or purple material forms specific shapes or morphotypes and is present to varying degrees throughout the light grey or orange matrix depending on the sample (Figures 2 and 4). Histograms of the pixel shades from tomograms show three main peaks which correspond to the two dominant components and the void space (Figure 3). Using the pixel shade, the electron densities and the material densities were calculated and used to identify the two dominant, non-void space components as well as the rare, high-density component that appears rarely in some regions of the matrix (Table 1).

The lightest grey material has an electron density of $0.77 \pm 0.02 e^-/\text{\AA}^3$ (average and 1SD of four samples), which corresponds to a density of $2.57 \pm 0.05 \text{ g/cm}^3$, similar to the mineral quartz, which has a density of 2.66 g/cm^3 . The lower density of the chert in our samples compared to quartz may be due to differences in crystallinity and/or porosity that are below the resolution of the measurement. The composition of the matrix is unsurprising given previous studies that used light microscopy and SEM with energy dispersive X-ray spectroscopy (EDS) to identify this material as chert, a microcrystalline SiO_2 (Moore et al. 2024). The density of this microcrystalline chert is quite uniform even across the two samples, indicating that the chert is homogenous and does not contain an abundance of accessory minerals. Rare exceptions are occasional white spots $< 1 \mu\text{m}$ across that are present within the chert in some regions. These have electron densities of $2.14 \pm 0.34 e^-/\text{\AA}^3$, corresponding to very high material densities of more than 7 g/cm^3 ; this rare nanophase may be Fe metal ($A/Z = 2.15$, with a material density of 7.9 g/cm^3).

The mid-toned grey component shows more variability across the samples and even across morphotypes. These regions have electron densities of $0.39 \pm 0.04 e^-/\text{\AA}^3$ (average and 1SD of four samples), which corresponds to material densities of $1.26 \pm 0.11 \text{ g/cm}^3$, values that are consistent with densities reported for kerogen which can have densities between 1.19 and 1.77 g/cm^3 (Bousige et al. 2016; Jagadisan et al. 2017; Maldanis et al. 2020; Okiongbo et al. 2005; Vandenbroucke and Largeau 2007). This is also consistent with light microscopy and SEM/EDS analyses which have identified

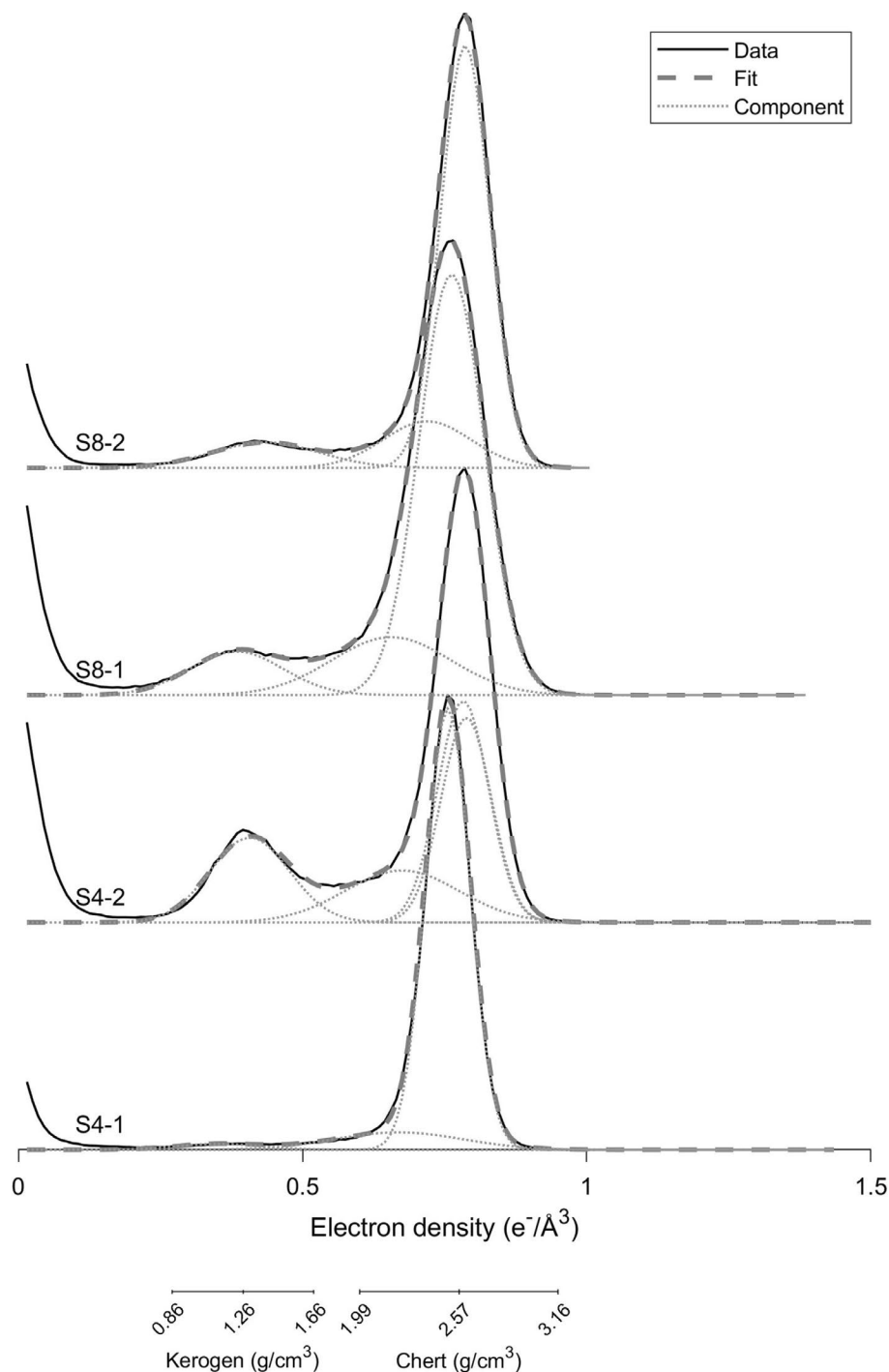


FIGURE 3 | Histograms of electron densities in 1 million randomly sampled voxels from each specimen (solid lines). Dashed lines are Gaussian mixture model fits to sampled electron densities, composed of three or four endmember components (dotted lines). Material densities of kerogen and chert are calculated using A/Z ratios of 1.92 and 2.00, respectively.

carbonaceous spherical structures interpreted as microfossils in these samples (Moore et al. 2024). The difference in density across morphotypes suggests greater heterogeneity in the material composition as compared to the chert. However, these values—although variable—all still fall within the broad ranges of kerogen. Void space is also present within the chert samples in association with some of the kerogenous material (Figures 2 and 4). Interestingly, the amount and distribution of void space is variable depending on the sample as well as the morphology of the structure, with some morphotypes

having a greater percentage of associated void space than others (Figure 4).

4.2 | Silica-Organic Textures

PXCT reveals striking nanoscale textural relationships between silica and kerogen within the microfossils that are not seen with conventional microscopic techniques. While all morphotypes appear to have continuous walls and dense,

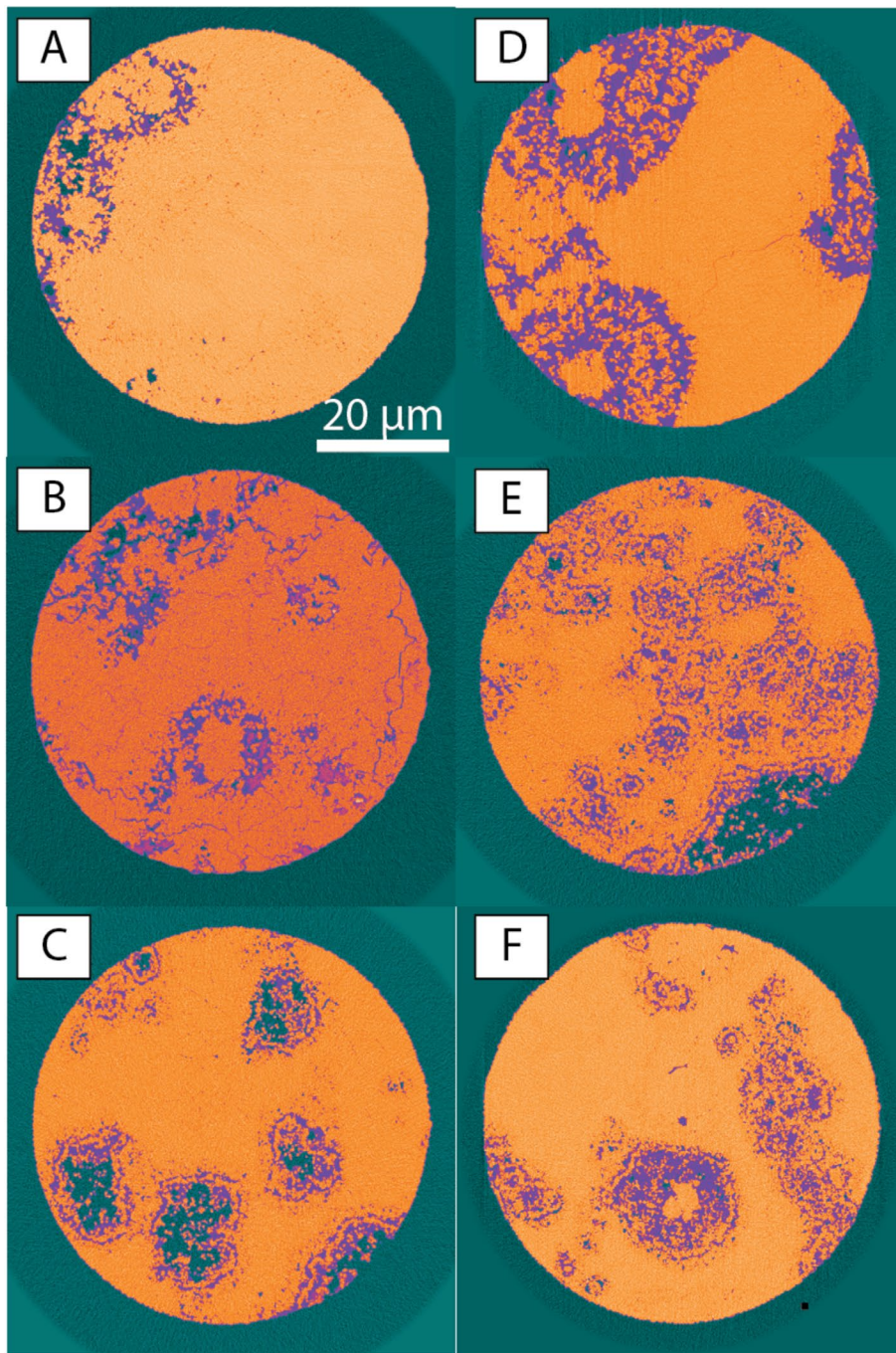


FIGURE 4 | Colorized illustrations of example axial tomographic slices distinguishing the 6 microfossil morphotypes (A = 1, B = 2, C = 4, D = 7, E = 10, F = 11) preserved within and across chert samples. Teal = void space, purple = kerogen, orange = chert.

uniformly organic matrices under transmitted light (Figure 1), the 2D axial tomographic slices (Figure 4) and 3D renderings (Figures 5 and 6) reveal that these structures are, in fact, a meshwork of organic matter and silica. Most of the chert in these samples consists of equant microcrystalline ($<5\mu\text{m}$) crystals that are often anhedral or subhedral. However, the silica that is intimately interwoven with the amorphous organic material is comprised of significantly smaller nanoparticle sizes (Figures 4 and 5). Rather than surrounding and encompassing the organic structures, the silica is intergrown with the kerogen, creating a reticulate web of kerogen embedded with silica nanoparticles between 500 nm and 1 μm (Figures 4

and 5). Silica nanoparticles may be isolated within the web of kerogen and also connected to other crystals and to the surrounding matrix (Figures 4 and 5). Also noteworthy is the lack of other accessory minerals associated with the microfossils. Although some small minerals with high densities are occasionally present in the chert matrix (e.g., Figure 2), the kerogen is only associated with silica (Figures 4 and 5). Depending on the sample and the microfossil morphotype, void space may also be associated with the kerogen-silica meshwork as isolated patches (Figures 4 and 5). In most cases, void space comprises only a small fraction of the microfossil walls and interiors, with one notable exception discussed below.

TABLE 1 | Electron densities, volumetric proportion (excluding voids), interpreted phase and associated ratio of molar mass to electron content (A/Z), and resultant material density of modal phases in each specimen. Voxels that were nanoscale mixtures of multiple phases required their own Gaussian component, and fitting the chert phase in specimen S4_2 required two Gaussian components (see data processing methods).

	[e ⁻ /Ångström ³]		[%]			[g/cm ³]	
	Mean	1SD	Proportion	Phase	A/Z	ρ	Color label in Figure 2
S4_1	0.352	0.077	2.3	Kerogen	1.92	1.12	B
	0.669	0.113	10.	Mixture			
	0.756	0.039	88	Chert	2.00	2.51	C
S4_2	0.407	0.070	20.	Kerogen	1.92	1.30	B
	0.675	0.100	17	Mixture			
	0.782	0.045	33	Chert (a)	2.00	2.60	C
	0.788	0.045	30	Chert (b)	2.00	2.62	C
	2.136	0.341	0.03	Fe (?)	2.15	7.61	D
S8_1	0.384	0.082	11	Kerogen	1.92	1.22	B
	0.656	0.104	18	Mixture			
	0.762	0.057	72	Chert	2.00	2.53	C
S8_2	0.435	0.094	9.9	Kerogen	1.92	1.39	B
	0.719	0.077	15	Mixture			
	0.786	0.042	75	Chert	2.00	2.61	C

The predominant organic nanostructures are ovoid balls approximately 100 nm in diameter, which are often hollow (Figure 5A). These typically form popcorn-textured aggregates up to several microns across. Sometimes, the ovoids have protruding arms or tubules. Other nanostructures are larger irregularly shaped sacs 300–1000 nm across their largest dimension, which are generally equant or amoeboid in shape (Figure 5B). Especially at the outer boundary of some microfossils, loose concentric cortices formed from sacs organized into chains of flattened, sinuous, chambers (Figure 5C) or reticulate networks of filled clots (Figure 5D). Finally, some kerogen lines subhedral chert crystallites (Figure 5E), which may represent aggrading neomorphic recrystallization of kerogen-chert aggregates.

4.3 | Microfossil Morphologies

The organic-rich structures analyzed in this study are among those previously characterized through petrographic analyses in Moore et al. (2024). Across chert samples from the Barra Velha Formation, 13 microfossil morphotypes were previously identified. The samples analyzed here contain 6 of these morphotypes (Figures 1 and 6 and Supp. videos S1–S5). In thin section, these morphotypes are distinguishable by their size ranges as well as some defining surface features and internal structures (Figure 1). Morphotype 1 fossils are ~5–10 μm diameter spheres that have a distinct dark, organic-rich wall. Morphotype 2 fossils also have a distinct outer wall, but their sizes range between ~10 and 20 μm in diameter. Both morphotypes 1 and 2 tend to occur in clusters in the microcrystalline chert distributed near carbonate intraclasts and throughout the chert matrix. Morphotype 4 fossils are also found abundantly distributed throughout the

microcrystalline chert matrix and are often found in clusters. These microfossils are ~10–15 μm in diameter but, unlike types 1 and 2, have dense opaque rather than chert-filled interiors and are surrounded by a thin organic halo with microcrystalline chert between the “halo” and the opaque interior. Morphotype 7 fossils are large structures with two concentric organic-rich envelopes with chert between the outer envelope and inside of the inner envelope, filling the structure’s interior. Morphotypes 10 and 11 are dense, organic-rich structures, though with different size ranges. Morphotype 10 is abundant throughout sample S8 and is found alongside many other morphotypes. These structures are typically found in clusters and are ~5–10 μm in diameter. Morphotype 11, on the other hand, is ~20–30 μm diameter and these structures are often surrounded by a rim of silica.

In 2D axial tomographic slices and 3D renderings, these 6 morphotypes were identifiable as distinct shapes composed of the mid-toned or false-colored purple kerogen material (Figures 4 and 6). To highlight the shapes of the organic material, 3D renderings were also generated of kerogen alone without chert, depicting the kerogen (and microfossils) in gold alongside the grey-scale reconstructions (Figures 5 and 6). In addition to patches of non-fossil kerogen—organic material preserved in the matrix that lacked distinct morphology—each of the distinct morphotypes described above was identified based on the size classes, presence or absence of organic walls, and presence or absence of organic matter in the interior of the structures (Figures 4–6). In addition to these general characteristics, tomograms revealed more nuanced textural and morphological differences across the morphotypes that were not previously visible through light microscopy alone. In particular, the amount of organic matter preserved, the thickness of the walls, the amount of

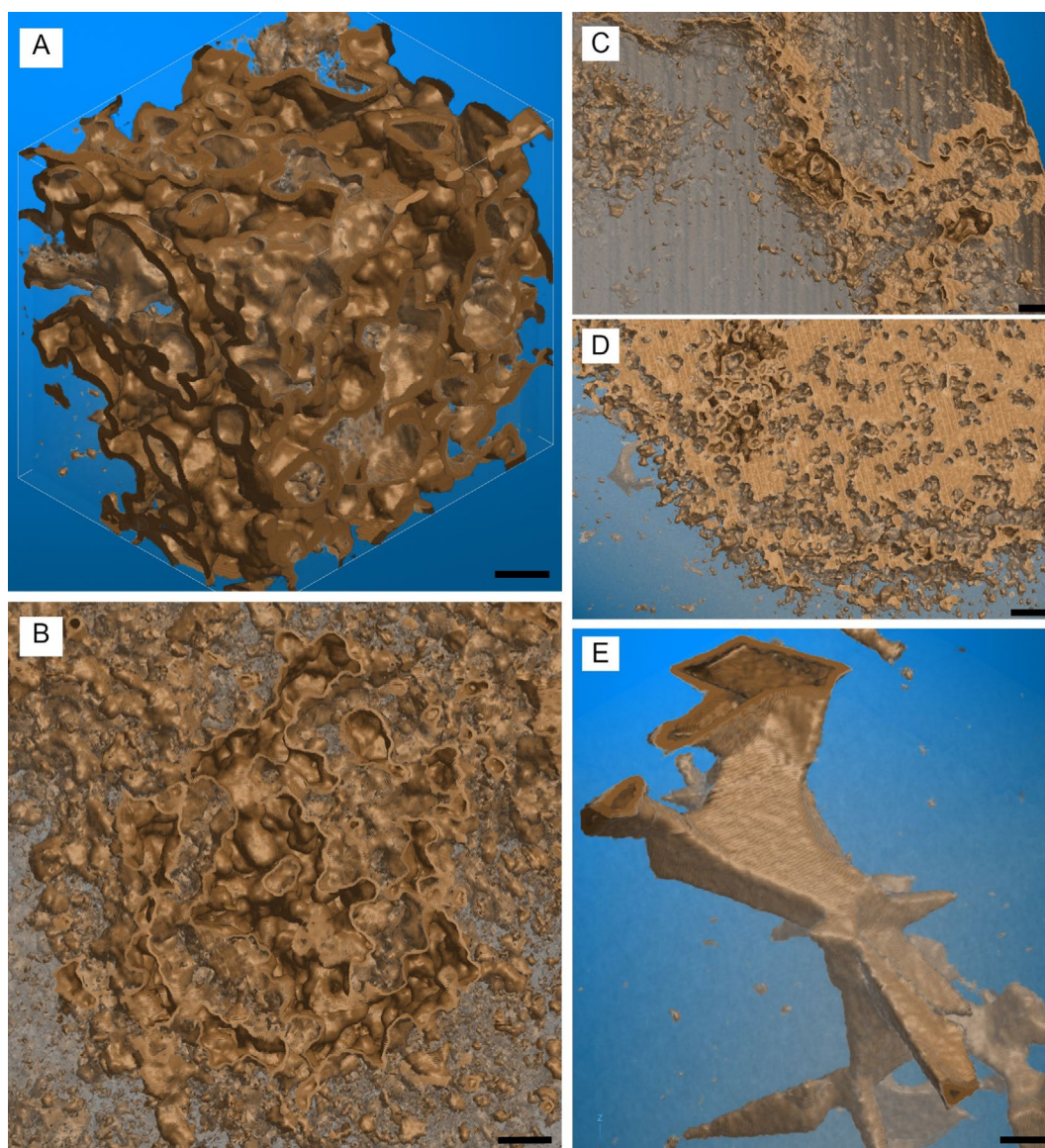


FIGURE 5 | Nanoscale kerogen microtextures. (A) Popcorn texture with hollow vesicles, S4-1. 500 nm scale bar. (B) Irregular sacs with scalloped and teardrop-shaped margins, S8-1. 500 nm scale bar. (C) Sinuous chain of pancake-shaped vesicles, S4-1. 1000 nm scale bar. (D) Reticulate pattern of open and filled clots, which are arranged in loose concentric sheets at the microfossil boundary, S8-2. 1000 nm scale bar. (E) Kerogen accumulated along euhedral quartz microcrystallites, S8-2. 500 nm scale bar.

void space associated with the organic material and structures, and the cross-sectional shapes of the structures were different across the morphotypes. Thus, this new technique allowed for significantly more detailed characterization of the structures, the microfossil diversity, and taphonomic variability than was previously possible.

Morphotype 1 and 2 microfossils, although characterized by different size ranges, have broadly similar morphologies and preservation styles. Both morphotypes have a thin organic wall with chert infilling the structure interior. In 2D axial tomographic slices and 3D renderings, it is apparent that the organic wall of these structures is thin (1–4 μm) and contains relatively little total organic matter (Figures 4A,B and 6A,B). The walls are comprised of roughly half organic matter and half silica with rare nanoscopic patches of void space. The structure interiors, on the other hand, are entirely composed of microcrystalline

chert. Even at the high resolution of the tomograms, both morphotypes 1 and 2 demonstrate a uniform circular cross-sectional morphology.

Morphotype 4 is quite different from 1 and 2 and is the major exception regarding void space. Morphotype 4 structures are surrounded with somewhat irregular shapes both in transmitted light (Figure 1) and in 2D axial tomographic slices (Figure 4C) and 3D renderings (Figure 6C). The outermost wall of morphotype 4 structures is a semi-continuous wall of a <1 μm thick layer of kerogen broken occasionally by silica nanoparticles. Between this thin outer layer, a thicker (~1 μm) layer of silica nanoparticles separates the wall from the structure interior. The innermost region of morphotype 4 structures shows some intergrowth of kerogen and silica. However, void space occupies the architecture of the inner space in morphotype 4, comprising ~75% of the structure interior and disrupted by nanoscopic silica

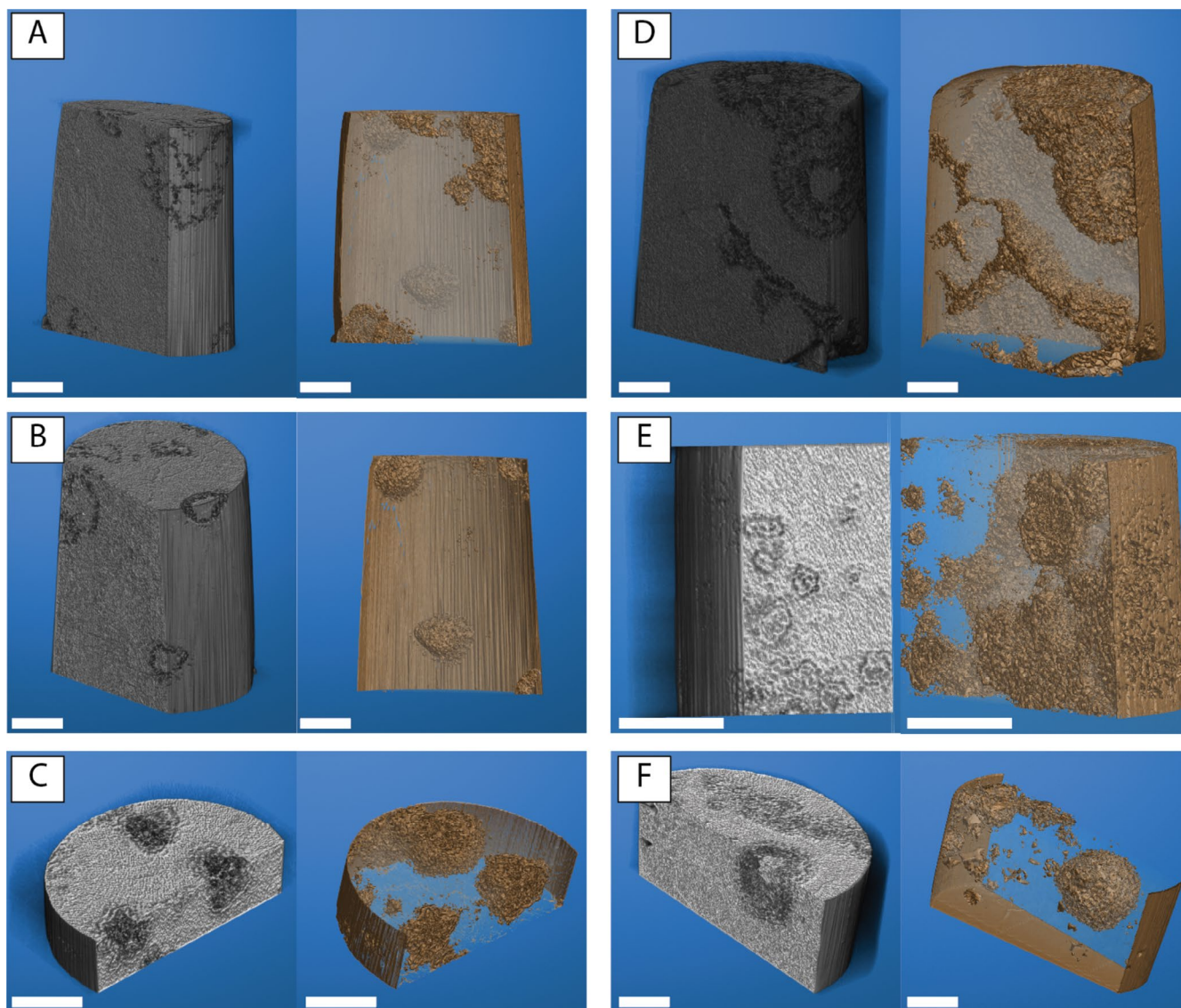


FIGURE 6 | 3D renderings depicting examples of the six microfossil morphotypes (A = 1, B = 2, C = 4, D = 7, E = 10, F = 11). For each morphotype, 3D renderings are depicted in grey-scale (left panels) illustrating the different materials (void space, kerogen, and chert) and in gold (right panels) illustrating the kerogen alone with chert and void-space removed to highlight the microfossil morphologies.

grains and kerogen patches. This distinct feature was not apparent from light microscopy alone but is clearly visible in 2D axial tomographic slices and 3D renderings (Figures 4C and 6C) and sets morphotype 4 structures apart from all other morphotypes.

Morphotype 7 represents the largest microfossils preserved in chert from the Barra Velha Formation. Like morphotypes 1 and 2, these are organic-walled structures, though they show some distinct features in addition to their size. First, rather than a single organic wall, these fossils have two concentric organic-rich walls and are filled with silica inside the inner-most organic wall. In thin section, these structures appeared to have a predominantly silica-rich layer between the two organic walls, but 2D axial tomographic slices and 3D renderings reveal that the space between the two densely organic walls is in fact an intergrowth of organic matter and silica nanoparticles (Figures 4D and 6D), similar to the silica-organic mesh in the other microfossils. However, the double walls and inter-wall space in morphotype 7 fossils contain more total organic matter compared to

morphotypes 1, 2, and 4. Like morphotypes 1 and 2, morphotype 7 structures have a uniform circular cross section and spherical 3D shape.

Morphotypes 10 and 11 are typically spatially associated with each other in thin section. Morphotype 10 appears to be quite abundant, and the individual structures are typically clustered in patches or chains (Figures 4E and 6E). These microfossils are small (~5–10 μm) like morphotype 1, and they also have a thin, organic-rich wall that is <1 μm thick. However, unlike morphotype 1, morphotype 10 fossils have an organic-rich interior and are separated from the outer wall by a thin, <1 μm layer of silica nanoparticles (Figures 4E and 6E). The innermost portion of the structure displays the same organic-silica mesh texture as the other microfossils. Morphotype 11 fossils are similar to 10 in that they are characterized by a <1 μm thick organic-rich outer wall, an organic-rich interior, and a <1 μm thick layer of silica nanoparticles between the two (Figures 4F and 6F). However, these microfossils

are much larger than morphotype 10 (~20–30 μm diameter), and they occur as isolated structures surrounded by chert. Additionally, the innermost portion of morphotype 10 fossils is more organic-rich than any of the other microfossils and appears more as an organic sphere with heterogeneously distributed silica nanoparticles rather than the meshwork of silica and organic matter that characterized the other microfossils (Figures 4F and 6F). These fossils sometimes have a single, small sphere of chert within the organic interior, generally slightly off from center (Figure 6F).

5 | Discussion

5.1 | Silica-Organic Textures and Implications for Taphonomic Mechanisms

Silica may precipitate in a variety of environments through different mechanisms depending on the water chemistry as well as, in some cases, the contributions of microbes and associated organic compounds in nucleating silica. Modern environmental and experimental studies have highlighted some of these mechanisms. However, it is often difficult to interpret the mechanisms, chemical conditions, and microbial-environmental interactions that may have been at play in past environments based on the rock and microfossil record alone. The results of this study provide exceptional nanoscale resolution imaging of fossiliferous chert that may help us bridge the gap between mechanisms observed in modern environments and experimental studies and potential mechanisms in ancient environments. In the rock record, microfossils preserved in chert have been documented in rock formations that sample different environments that likely experienced different chemical conditions and, as a result, followed different mechanisms of silicification (e.g., Demoulin et al. 2019; Moore et al. 2023; Schopf and Klein 1992; Sergeev and Sharma 2012 and references therein). For example, microfossiliferous chert from the Proterozoic is frequently found in shallow marine deposits (Schopf and Klein 1992; Sergeev and Sharma 2012; Butterfield 2015; Demoulin et al. 2019; Moore et al. 2023) while younger deposits like the Devonian Rhynie Chert formed in restricted terrestrial environments associated with hydrothermal activity (Rice et al. 2002; Edwards et al. 2018; Garwood et al. 2019; Strullu-Derrien et al. 2019). Silica has also been documented in recent and modern environments, including opal speleothems and microbialites that form in caves in Venezuela and the Czech Republic (Aubrecht et al. 2008; Sauro et al. 2018; Suchý et al. 2021) and silica phases associated with recent hydrothermal systems in the Andes (e.g., Slagter et al. 2019; Gong et al. 2020). In these cases, the silica that preserves microbes and microfossils is a microcrystalline chert or (in the case of recent deposits) amorphous silica or opal.

Although the conditions and mechanisms of chert formation in Proterozoic marine environments, modern and ancient terrestrial hydrothermal environments, or freshwater systems are very different, they share some important features. Across these environments, the silica must have precipitated rapidly from solution to preserve the organic material and the morphology of the delicate microbial cells before they could be

degraded. This is evidenced by the preservation of the fossils and kerogen (Schopf and Klein 1992; Rice et al. 2002; Sergeev and Sharma 2012; Butterfield 2015; Edwards et al. 2018; Demoulin et al. 2019; Garwood et al. 2019; Strullu-Derrien et al. 2019; Moore et al. 2023) and further corroborated by modern experimental studies that investigate rates of organic decay in microbial communities (e.g., Stout et al. 2014). These experiments reveal that organic degradation can take place on the order of hours or days (Stout et al. 2014). Under the right conditions, though, silica precipitation could outpace organic degradation and facilitate preservation of microfossil morphologies and kerogen. Analysis of microfossils preserved in the Barra Velha Formation reveals that (1) both kerogen and body fossil morphologies are preserved in the form of organic-rich wall and (2) some degree of diversity is apparent in the structures at the micro- to nanoscale. This indicates that the mechanism of silicification in the pre-salt basin must have been a rapid process, similar to the mechanisms that characterized Proterozoic shallow marine environments and hydrothermal environments like the Rhynie Chert. To preserve this type of cellular detail that allows for distinction of different fossil groups, cells must have been preserved on the order of hours or days, pointing to rapid silica polymerization prior to degradation.

In addition to the rapid rate of silica precipitation, the microcrystalline nature of the chert is a key feature related to preservation potential. Microorganisms preserved by chert are typically <200 μm and may include a range of bacteria and simple eukaryotes (e.g., Koch and Ehrenfeld 1968; Knoll 2014; Demoulin et al. 2019 and references therein). It is well documented that the fossiliferous rocks that we see today are characterized by microcrystalline chert matrices with crystals <5 μm . However, the primary silica phases from which the fossil-preserving microcrystalline chert developed, the compositions and crystalline-to-amorphous nature of these primary silica phases, and the mechanisms by which they formed and preserved kerogen and microfossils remain poorly constrained. Furthermore, although the matrix chert is well characterized in many fossiliferous chert deposits, the structural relationship between organic matter and silica is difficult to characterize at the nanoscale immediately around the microfossils, further complicating evaluation of the mechanism(s) of preservation.

Modern environments and experimental work provide some insights into potential ancient mechanisms of organic preservation by chert. In most modern aqueous environments, silica does not polymerize and precipitate abiotically because silica concentrations are generally low compared to ancient environments (μM concentrations compared to the ~1 mM silica estimated for Proterozoic seawater; Siever 1992; Tréguer et al. 1995; Maliva et al. 2005; Knoll 2008; Conley et al. 2017). However, some rare environments and experimental studies provide a window through which to study silica precipitation and microbial preservation. One type of modern silicification occurs in hydrothermal environments such as the hot springs of Yellowstone (Walter et al. 1972; Ferris et al. 1986; Cady and Farmer 1996), New Zealand (Jones and Renaut 1996; Jones et al. 1997, 1998, 2001, 2004, 2005; Campbell et al. 2002, 2015), Iceland (Schultze-Lam et al. 1995; Konhauser and Ferris 1996; Konhauser and Urrutia 1999; Konhauser et al. 2001), and the

Andes (Gong et al. 2020; Wilmeth et al. 2021), among others. The silica in these environments is sourced from hydrothermal fluids that contain elevated concentrations of silica (> 2 mM) as a result of water-rock interactions between the hydrothermal fluid and the silica-rich basement rocks through which it flows. At these elevated temperatures, silica solubility is elevated, allowing for exceptionally high concentrations of dissolved silica in the fluid. When the fluid reaches the surface, it cools as it flows away from the source, lowering silica solubility and resulting in rapid, abiotic silica precipitation. The silica that precipitates in these environments is typically opal-A, a hydrated, amorphous silica phase that often precipitates in the form of silica nanospheres or colloids < 1 µm in diameter (Walter et al. 1972; Ferris et al. 1986; Schultze-Lam et al. 1995; Jones and Renaut 1996; Konhauser and Ferris 1996; Jones et al. 1997, 1998, 2001, 2004, 2005; Konhauser and Urrutia 1999; Konhauser et al. 2001; Campbell et al. 2002, 2015; Cady and Farmer 1996; Gong et al. 2020; Wilmeth et al. 2021). Silica has also been observed in some modern and recent cave systems where it is suggested that the formation of silica speleothems is driven by microbially mediated dissolution and reprecipitation of silica; this process also results in the formation of amorphous silica or opal that preserves microbial structures and cells (Aubrecht et al. 2008; Sauro et al. 2018; Suchý et al. 2021).

The nanoscopic size of precipitates from these modern and recent environments (both hot spring systems and caves) and their amorphous nature allows them to preserve the shapes of microbial cells exceptionally well because the size of the precipitates is much smaller than the size of the cell. This allows for the preservation of nanoscopic features and delicate organic material without overprinting or destroying the cells. The preservation of the cellular morphology demonstrates the importance of the nanoscopic size of silica precipitates in microfossil preservation. Indeed, many of these studies suggest that, even when silica concentrations are high enough to facilitate abiotic silica polymerization, the cell surfaces and organic compounds may act as nucleation sites to promote silica precipitation (e.g., Schultze-Lam et al. 1995; Jones and Renaut 2003).

Experimental studies have uncovered additional key contributing factors to the preservation of microfossils and kerogen that may explain microfossil preservation in ancient environments. Like the silica that precipitates in modern hydrothermal environments and cave systems, the silica that has been observed in laboratory experiments is typically an amorphous phase that precipitates as nanoscopic colloidal particles (Francis, Barghoorn, et al. 1978; Francis, Margulis, et al. 1978; Westall 1995; Toporski et al. 2002; Benning et al. 2004; Orange et al. 2009; Moore et al. 2020, 2021, 2022). Again, as a result of the amorphous and nanoscopic nature of the precipitates, these precipitates preserve cellular features and sometimes the delicate organic material exceptionally well (Francis, Barghoorn, et al. 1978; Francis, Margulis, et al. 1978; Westall 1995; Toporski et al. 2002; Benning et al. 2004; Moore et al. 2020, 2021; Wilmeth et al. 2021). In addition to the size and amorphous nature of the precipitates, some experimental studies also demonstrate the importance of silica nucleation on the cell surfaces. As has been suggested in some hot

spring environments (e.g., Schultze-Lam et al. 1995; Jones and Renaut 2003), experimental studies have revealed that certain microbes can facilitate the nucleation of amorphous, nanoscopic silica colloids directly on the cell surfaces through organic-ion interactions (Francis, Barghoorn, et al. 1978; Francis, Margulis, et al. 1978; Urrutia and Beveridge 1993, 1994; Westall 1995; Konhauser et al. 2004; Lalonde et al. 2005; Moore et al. 2020). Importantly, when silica concentrations are below saturation and silica cannot precipitate abiotically, these organic nucleation sites become even more essential in facilitating silica precipitation (e.g., Moore et al. 2021, 2020).

These various modern environments and experimental studies have highlighted key features of different silica-precipitating mechanisms that may relate to microfossil preservation in ancient environments. However, it has been difficult to directly link these modern observations to ancient environments and silica-precipitation mechanisms for several reasons. First, although the silica that precipitates in modern environments and experiments is an amorphous phase, the fossil preserving chert that we see today is likely the product of a sequence of recrystallization processes that transform an originally amorphous phase into microcrystalline quartz (e.g., Saminpanya and Sutherland 2013 and references therein). This recrystallization process makes it difficult to assess the primary organic-silica fabrics. Second, the techniques that are typically used to characterize microfossils (e.g., light microscopy or SEM) do not allow for imaging of the organic-silica fabrics at high enough resolution to fully characterize these fabrics and the relationships of these phases in the areas immediately within and around the microfossils. Analysis of the microfossils preserved in chert from the Barra Velha Formation using PXCT furthers our understanding of silica-organic interactions preserved in the fossil record by generating nanoscale resolution imaging of microfossils that provide a novel perspective on their taphonomy.

Both the 2D axial tomographic slices and 3D renderings reveal key textural characteristics that help to link silica-organic interactions in modern environments and experiments to the fossil record. Although petrographic analyses typically characterize the microcrystalline nature of chert matrices that host microfossils, the nanoscale resolution achieved through PXCT reveals that the silica that surrounds and encases (and even permeates) the microfossils is, in fact, rounded silica nanoparticles. These key results shed light on the mechanisms that allowed for detailed sub-cellular and organic preservation because they demonstrate that, like the silica that precipitates in modern hydrothermal environments and experimental studies, the silica that drove initial preservation of the kerogen and microfossils was nanocrystalline to amorphous. Importantly, although the silica in the matrix likely underwent recrystallization from an amorphous precursor to the microcrystalline quartz that we see today, the silica associated with kerogen and microfossils retained a nanoscopic size (either nanocrystalline or amorphous). This suggests that preservation of microfossils in at least some environments likely began with the precipitation of an amorphous, nanoparticulate silica phase that stabilized the organic material and preserved the shapes of the cells. Such a mechanism has been hypothesized in the past, and our results here provide evidence to corroborate

these hypotheses. Additionally, the textural relationships between the kerogen and the silica in the walls of the microfossils suggest that, as observed in experimental studies, the silica that preserved the microfossils may have nucleated directly onto the organic matter, allowing for preservation of both the shapes of the cells and of the kerogen.

5.2 | Morphological Differences and Implications for Taxonomy and Taphonomy

Morphological differences among microfossils may be related to primary physiological differences among different soft-bodied organisms from ancient microbial communities. For example, bacterial and eukaryotic organisms may exhibit different size ranges, degrees of morphological complexity, and compositional differences in their cell membranes and walls (e.g., Javaux 2007; Knoll 2014 and references therein). It is also possible that morphological differences may relate to differences in the post-mortem processes that fossilized the soft-bodied organisms, or to a combination of primary and taphonomic processes. As such, it is critical to understand the processes and mechanisms that preserved a microfossil or microfossil community in order to accurately assess the contributions of primary and diagenetic morphological differences. Our PXCT analysis of microfossils in the Barra Velha Formation provides novel and unparalleled compositional and textural insight into the taphonomy and morphological variability across different microfossils within a given assemblage.

Petrographic analyses with light microscopy and SEM/EDS demonstrated that microfossils within and across chert-rich facies in the Barra Velha Formation show variability in size and some other morphological features (Moore et al. 2024). For example, some microfossils are characterized as hollow, organic-walled spheres while others have dense organic interiors or layers of concentric walls. Using PXCT, we gain further insight into these textural and compositional differences at greater resolution. First, 2D axial tomographic slices and 3D renderings reveal that although all microfossils appeared uniformly round in thin section, there is variability in the smoothness of the microfossils. The tomograms show that while morphotypes 1, 2, 7, and 11 are uniformly round, morphotypes 4 and 10 are quite irregularly shaped. Additionally, the tomograms of sample S8 reveal that morphotype 4, which appeared to be composed of densely packed organic material under transmitted light, is, in fact, hollow with void space in the center and surrounded by an organo-silica wall. These and other morphological and compositional differences, like the amount of organic matter preserved in 1, 2, and 4 versus 7, 10, and 11, may relate to (1) true morphological variability across different organisms, (2) taphonomic differences, or (3) a combination of taxonomic and taphonomic differences driven by primary morphological, physiological, or chemical differences across different organisms. Here, we consider all of these factors and their contributions to textural and chemical variability across fossil morphotypes.

Although the absolute size of a microfossil may not accurately reflect the size of the original organism (Francis, Barghoorn, et al. 1978; Francis, Margulis, et al. 1978; Jones and Renaut 1996;

Jones et al. 1997, 2001, 2005; Konhauser et al. 2004), the relative sizes of the microfossils in the Barra Velha Formation may represent size variability across different organisms. This is because all microfossils within a given sample were preserved in the same environment under the same conditions (Moore et al. 2024). As such, even if the structures were shrunk or enlarged by the fossilization process, they all would have been altered by similar factors meaning that they would retain—to some degree—the relative differences in size. By the same logic, the variability in smoothness of the microfossils may also be a true representation of variability in the shapes of the organisms. In these cases, the morphological variability in both size and shape of the microfossils represents a taxonomic end member explanation (explanation 1). Alternatively, the variability in size and morphology may be entirely the result of taphonomic variability (explanation 2). In this case, the different microfossil morphotypes may all represent the same type of organism but at different stages of degradation relative to silica precipitation. For example, the irregular shape of morphotype 4 alongside the hollow interiors that are not filled with silica may be due to collapse of the cell wall in cells that were partially degraded at the time of silica precipitation.

The third possibility is that the morphological and textural differences across morphotypes arise from a combination of taxonomic and taphonomic differences (explanation 3). In this case, the variability in preservation of different morphotypes may have been driven by differences in surface chemistry or physiology across different organisms which fostered variability in the organic-silica interactions as well as the rates of degradation relative to preservation. For example, organisms with more recalcitrant cell walls or envelopes may be preserved with a greater amount of organic matter compared to those with cell envelopes composed of highly labile organic compounds (e.g., Butterfield 1990). Alternatively, the specific organic compounds in the cell walls or envelopes of different organisms may have had different binding capacity or affinity for silica. For example, experimental studies and observations from modern hot spring environments have suggested that certain functional groups of classes of organic compounds more readily bind silica than others, leading to preferential preservation of certain organisms by silica (e.g., Francis, Barghoorn, et al. 1978; Francis, Margulis, et al. 1978; Urrutia and Beveridge 1994, 1993; Westall 1995; Phoenix et al. 2000; Yee et al. 2003; Konhauser et al. 2004; Lalonde et al. 2005; Orange et al. 2009; Moore et al. 2021). Whether related to recalcitrance or silica-binding capacity, variability in cell chemistry and organism physiology could explain, for example, the variability in the wall thickness of different morphotypes or why some morphotypes have hollow interiors and others are infilled with silica. Similarly, these factors could explain the differences in the amount of organic material preserved in the cell walls of 1, 2, and 4 versus 7, 10, and 11 or the preservation of a single outer wall versus multiple layers of walls or dense organic interiors. Thus, the morphological differences observed could reflect a combination of taxonomic and taphonomic variability. Based on the diversity in morphology, composition, textures, and degree of preservation, we favor this combined explanation and suggest that this assemblage represents at least some degree of true diversity with multiple different types of organisms preserved, but likely also reflects organism-specific taphonomic variability.

6 | Conclusions

High resolution, 3D characterization of chert-hosted microfossils from the Barra Velha Formation provides new insight into the mechanisms and organic-environmental interactions that facilitated biosignature preservation by silica in ancient environments, including the ancient alkaline lake of the pre-salt basin. Using PXCT to generate 2D axial tomographic slices and 3D renderings at nanoscale resolution, we present detailed visualizations of silica-organic relationships, microfossil morphologies, and taphonomic variability that clarify mechanisms of ancient microfossil preservation. At this resolution, both 2D and 3D visualizations reveal that microfossils are comprised of intergrown webs of kerogen and nanoscopic, subrounded silica particles that differ in size, shape, and texture from the surrounding matrix, which is composed of microcrystalline chert.

Previous studies investigating silicification through laboratory experiments and in modern environments have long suggested that silicification in ancient environments involved amorphous, colloidal silica precipitation and may have involved nucleation of these earliest silica phases on cell surfaces and organic compounds. However, connecting these modern insights to the past has been difficult due to resolution limitations and uncertainty surrounding the phase transitions between opaline and crystalline silica phases. The nanoscopic shapes, sizes, and textures of the silica and silica-organic fabrics observed using PXCT are consistent with colloidal silica precipitates that have been observed in association with cells and organic material in modern silica-rich environments and laboratory experiments. These observations allow for direct comparison between organo-silica textures in modern and fossil organisms and help to support the link between modern observations and ancient taphonomic processes in environments like the pre-salt basin. We suggest that silicification in the pre-salt basin occurred through a similar mechanism of colloidal, amorphous silica precipitation. Within this mechanism, the key to the preservation of organic matter and cellular morphologies was rapid nucleation of silica on organic compounds and cell surfaces.

In addition to insights into organo-silica textures and fabrics, the 3D visualizations obtained through PXCT illustrate the different fossil morphotypes in a way that would not have been otherwise detected through traditional petrographic analyses. Some morphological and textural variability may be the result of taphonomic variability in which the relative amounts of silica, kerogen, and void space as well as the degree of fossil “roundness” relates to the timing of silica nucleation relative to organic degradation. However, the variability in size, microfossil wall thickness, and internal and wall composition apparent across microfossils preserved within a given sample points to additional variability reflective of primary differences across different organisms. We therefore suggest that the microfossil assemblage preserved within the Barra Velha Formation chert represents a diverse group of microbial organisms that exhibit morphological, physiological, and taphonomic variability. Importantly, the combination of taxonomic and taphonomic variability apparent in these samples points to potential differences in the chemistry and physiology of the different microbes and, as a result, differences in silica-organic interactions. Further experimental work and microfossil analyses that investigate if and how different

organisms and organic compounds interact with dissolved silica and facilitate silica precipitation may shed light on the relationships between taxonomy and taphonomy of microbial organisms. These constraints will allow us to better characterize ancient fossil assemblages like the microfossils preserved in the Barra Velha Formation as well as those preserved in chert from different environments throughout Earth history.

Acknowledgements

Funding for this project was provided by the Simons Foundation through a grant to JPG and the Paul Scherrer Institute Swiss Light Source. We thank Shell for providing samples and J. Reuteler for sample preparation at the Scientific Center for Optical Microscopy (ScopeM) facility at ETH Zurich. PXCT measurements were carried out at the cSAXS beamline, Paul Scherrer Institute, Switzerland. Additional thanks to E. Adams, R. Newport, L. Fadel Cury, A. Bahniuk, and H. Albrecht for helpful conversations and to D. Hutkin for support.

Conflicts of Interest

The authors declare no conflicts of interest.

Data Availability Statement

The data and code that support the findings of this study are archived by CaltechDATA at <https://doi.org/10.22002/xybt1-wpg62> (Moore et al. 2025).

References

- Aubrecht, R., C. Brewer-Carías, B. Šmída, M. Audy, and L. Kováčik. 2008. “Anatomy of Biologically Mediated Opal Speleothems in the World’s Largest Sandstone Cave: Cueva Charles Brewer, Chimantá Plateau, Venezuela.” *Sedimentary Geology* 203: 181–195.
- Benning, L. G., V. R. Phoenix, N. Yee, and M. J. Tobin. 2004. “Molecular Characterization of Cyanobacterial Silicification Using Synchrotron Infrared Micro-Spectroscopy.” *Geochimica et Cosmochimica Acta* 68: 729–741.
- Bousige, C., C. M. Ghimbeu, C. Vix-Guterl, et al. 2016. “Realistic Molecular Model of Kerogen’s Nanostructure.” *Nature Materials* 15: 576–582.
- Butterfield, N. J. 1990. “Organic Preservation of Non-Mineralizing Organisms and the Taphonomy of the Burgess Shale.” *Paleobiology* 16: 272–286.
- Butterfield, N. J. 2015. “Proterozoic Photosynthesis—A Critical Review.” *Palaeontology* 58: 953–972.
- Cady, S. L., and J. D. Farmer. 1996. “Fossilization Processes in Siliceous Thermal Springs: Trends in Preservation Along Thermal Gradients.” *Ciba Foundation Symposium* 202: 150–170; discussion 170–173. <https://doi.org/10.1002/9780470514986.ch9>.
- Campbell, K. A., B. Y. Lynne, K. M. Handley, et al. 2015. “Tracing Biosignature Preservation of Geothermally Silicified Microbial Textures Into the Geological Record.” *Astrobiology* 15: 858–882.
- Campbell, K. A., K. A. Rodgers, J. M. A. Brotheridge, and P. R. L. Browne. 2002. “An Unusual Modern Silica–Carbonate Sinter From Pavlova Spring, Ngatamariki, New Zealand.” *Sedimentology* 49: 835–854.
- Carminatti, M., B. Wolff, and L. Gamboa. 2008. *New Exploratory Frontiers in Brazil*. World Petroleum Congress.
- Carramal, N. G., D. M. Oliveira, A. S. M. Cacula, et al. 2022. “Paleoenvironmental Insights From the Deposition and Diagenesis of Aptian Pre-Salt Magnesium Silicates From the Lula Field, Santos Basin,

- Brazil." *Journal of Sedimentary Research* 92, no. 1: 12–31. <https://doi.org/10.2110/jsr.2020.139>.
- Conley, D. J., P. J. Frings, G. Fontorbe, et al. 2017. "Biosilicification Drives a Decline of Dissolved Si in the Oceans Through Geologic Time." *Frontiers in Marine Science* 4: 1–19.
- Demoulin, C. F., Y. J. Lara, L. Cornet, et al. 2019. "Cyanobacteria Evolution: Insight From the Fossil Record." *Free Radical Biology and Medicine* 140: 206–223.
- Diaz, A., B. Malkova, M. Holler, et al. 2015. "Three-Dimensional Mass Density Mapping of Cellular Ultrastructure by Ptychographic X-Ray Nanotomography." *Journal of Structural Biology* 192: 461–469.
- Dierolf, M., A. Menzel, P. Thibault, et al. 2010. "Ptychographic X-Ray Computed Tomography at the Nanoscale." *Nature* 467: 436–439.
- Edwards, D., P. Kenrick, and L. Dolan. 2018. "History and Contemporary Significance of the Rhynie Cherts—Our Earliest Preserved Terrestrial Ecosystem." *Philosophical Transactions of the Royal Society, B: Biological Sciences* 373: 1–7.
- Ferris, F. G., T. J. Beveridge, and W. S. Fyfe. 1986. "Iron-Silica Crystallite Nucleation by Bacteria in a Geothermal Sediment." *Nature* 320: 609–611.
- Ferris, F. G., W. S. Fyfe, and T. J. Beveridge. 1988. "Metallic Ion Binding by *Bacillus subtilis*: Implications for the Fossilization of Microorganisms." *Geology* 16: 149–152.
- Francis, S., E. S. Barghoorn, and L. Margulis. 1978. "On the Experimental Silicification of Microorganisms. III. Implications of the Preservation of the Green Prokaryotic Alga *Prochloron* and Other Coccolids for Interpretation of the Microbial Fossil Record." *Precambrian Research* 7: 377–383.
- Francis, S., L. Margulis, and E. S. Barghoorn. 1978. "On the Experimental Silicification of Microorganisms II. On the Time of Appearance of Eukaryotic Organisms in the Fossil Record." *Precambrian Research* 6: 65–100.
- Garwood, R. J., H. Oliver, and A. R. T. Spencer. 2019. "An Introduction to the Rhynie Chert." *Geological Magazine* 157: 47–64.
- Gong, J., K. D. Myers, C. Munoz-Saez, et al. 2020. "Formation and Preservation of Microbial Palisade Fabric in Silica Deposits From El Tatio, Chile." *Astrobiology* 20, no. 4: 500–524. <https://doi.org/10.1089/ast.2019.2025>.
- Guizar-Sicairos, M., A. Diaz, M. Holler, et al. 2011. "Phase Tomography From X-Ray Coherent Diffractive Imaging Projections." *Optics Express* 19: 21345–21357.
- Guizar-Sicairos, M., I. Johnson, A. Diaz, et al. 2014. "High-Throughput Ptychography Using Eiger: Scanning X-Ray Nano-Imaging of Extended Regions." *Optics Express* 22: 14859–14870.
- Holler, M., M. Guizar-Sicairos, E. H. R. Tsai, et al. 2017. "High-Resolution Non-Destructive Three-Dimensional Imaging of Integrated Circuits." *Nature* 543: 402–406.
- Holler, M., J. Raabe, A. Diaz, et al. 2012. "An Instrument for 3D X-Ray Nano-Imaging." *Review of Scientific Instruments* 83: 73703.
- Huang, X., H. Yan, R. Harder, Y. Hwu, I. K. Robinson, and Y. S. Chu. 2014. "Optimization of Overlap Uniformness for Ptychography." *Optics Express* 22: 12634–12644.
- Jagadisan, A., A. Yang, and Z. Heidari. 2017. "Experimental Quantification of the Impact of Thermal Maturity on Kerogen Density." *Petrophysics* 58: 603–612.
- Javaux, E. J. 2007. "The Early Eukaryotic Fossil Record." In *Eukaryotic Membranes and Cytoskeleton, Advances in Experimental Medicine and Biology*, 1–19. Springer.
- Jones, B., K. O. Konhauser, R. W. Renault, and R. S. Wheeler. 2004. "Microbial Silicification in Iodine Pool, Waimangu Geothermal Area, North Island, New Zealand: Implications for Recognition and Identification of Ancient Silicified Microbes." *Journal of the Geological Society* 161: 983–993.
- Jones, B., R. Renault, and M. Rosen. 2001. "Taphonomy of Silicified Filamentous Microbes in Modern Geothermal Sinters—Implications for Identification." *Palaios* 16: 580–592.
- Jones, B., and R. W. Renault. 1996. "Influence of Thermophilic Bacteria on Calcite and Silica Precipitation in Hot Springs With Water Temperatures Above 90°C: Evidence From Kenya and New Zealand." *Canadian Journal of Earth Sciences* 33: 72–83.
- Jones, B., and R. W. Renault. 2003. "Hot Spring and Geyser Sinters: The Integrated Product of Precipitation, Replacement, and Deposition." *Canadian Journal of Earth Sciences* 40: 1549–1569.
- Jones, B., R. W. Renault, and K. O. Konhauser. 2005. "Genesis of Large Siliceous Stromatolites at Frying Pan Lake, Waimangu Geothermal Field, North Island, New Zealand." *Sedimentology* 52: 1229–1252.
- Jones, B., R. W. Renault, and M. R. Rosen. 1997. "Biogenicity of Silica Precipitation Around Geysers and Hot-Spring Vents, North Island, New Zealand." *Journal of Sedimentary Research* 67: 88–104.
- Jones, B., R. W. Renault, and M. R. Rosen. 1998. "Microbial Biofacies in Hot-Spring Sinters; a Model Based on Ohaaki Pool, North Island, New Zealand." *Journal of Sedimentary Research* 68: 413–434.
- Kaestner, A., B. Münch, P. Trtlk, and L. Butler. 2011. "Spatiotemporal Computed Tomography of Dynamic Processes." *Optical Engineering* 50: 201.
- Knoll, A. H. 2008. *The Cyanobacteria: Molecular Biology, Genomics and Evolution*. Caister Academic Press.
- Knoll, A. H. 2014. "Paleobiological Perspectives on Early Eukaryotic Evolution." *Cold Spring Harbor Perspectives in Biology* 6, no. 1: 1–14. <https://doi.org/10.1101/cshperspect.a016121>.
- Knoll, A. H., S. Wörndle, and L. C. Kah. 2013. "Covariance of Microfossil Assemblages and Microbialite Textures Across an Upper Mesoproterozoic Carbonate Platform." *Palaios* 28: 453–470.
- Koch, A. L., and E. Ehrenfeld. 1968. "The Size and Shape of Bacteria by Light Scattering Measurements." *Biochimica et Biophysica Acta (BBA) - General Subjects* 165: 262–273.
- Konhauser, K. O., and F. G. Ferris. 1996. "Diversity of Iron and Silica Precipitation by Microbial Mats in Hydrothermal Waters, Iceland: Implications for Precambrian Iron Formations." *Geology* 24: 323.
- Konhauser, K. O., B. Jones, V. R. Phoenix, F. G. Ferris, and R. W. Renault. 2004. "The Microbial Role in Hot Spring Silicification." *Ambio* 33: 552–558.
- Konhauser, K. O., V. R. Phoenix, S. H. Bottrell, D. G. Adams, and I. M. Head. 2001. "Microbial–Silica Interactions in Icelandic Hot Spring Sinter: Possible Analogues for Some Precambrian Siliceous Stromatolites." *Sedimentology* 48: 415–433.
- Konhauser, K. O., and M. M. Urrutia. 1999. "Bacterial Clay Authigenesis: A Common Biogeochemical Process." *Chemical Geology* 161: 399–413.
- Lalonde, S. V., K. O. Konhauser, A.-L. Reysenbach, and F. G. Ferris. 2005. "The Experimental Silicification of Aquificales and Their Role in Hot Spring Sinter Formation." *Geobiology* 3: 41–52.
- Maldanis, L., K. Hickman-Lewis, M. Verezhak, et al. 2020. "Nanoscale 3D Quantitative Imaging of 1.88 Ga Gunflint Microfossils Reveals Novel Insights Into Taphonomic and Biogenic Characters." *Scientific Reports* 10: 8163.
- Maliva, R. G., A. H. Knoll, and B. M. Simonson. 2005. "Secular Change in the Precambrian Silica Cycle: Insights From Chert Petrology." *Geological Society of America Bulletin* 117: 835–845.
- Manning-Berg, A. R., and L. C. Kah. 2017. "Proterozoic Microbial Mats and Their Constraints on Environments of Silicification." *Geobiology* 15: 469–483.

- Manning-Berg, A. R., L. C. Kah, and K. H. Williford. 2018. "Evaluation of Preliminary Techniques Used to Assess Taphonomic Variation in Silicified Microbial Mats Preserved in the Angmaat Formation, Northern Baffin Island, Nunavut 10."
- Manning-Berg, A. R., R. S. Wood, K. H. Williford, A. D. Czaja, and L. C. Kah. 2019. "The Taphonomy of Proterozoic Microbial Mats and Implications for Early Diagenetic Silicification." *Geosciences* 9: 40.
- Mercedes-Martín, R., C. Ayora, J. Tritilla, and M. Sánchez-Román. 2019. "The Hydrochemical Evolution of Alkaline Volcanic Lakes: A Model to Understand the South Atlantic Pre-Salt Mineral Assemblages." *Earth-Science Reviews* 198: 1–19.
- Moore, K. R., A. Crémière, T. M. Present, et al. 2024. "Primary Microfossiliferous Chert in the Aptian Barra Velha Formation." *Sedimentology* 71: 1815–1842.
- Moore, K. R., M. Daye, J. Gong, K. Williford, K. Konhauser, and T. Bosak. 2023. "A Review of Microbial-Environmental Interactions Recorded in Proterozoic Carbonate-Hosted Chert." *Geobiology* 21: 3–27.
- Moore, K. R., J. Gong, M. Pajusalu, et al. 2021. "A New Model for Silicification of Cyanobacteria in Proterozoic Tidal Flats." *Geobiology* 19: 438–449.
- Moore, K. R., M. Pajusalu, J. Gong, et al. 2020. "Biologically Mediated Silicification of Marine Cyanobacteria and Implications for the Proterozoic Fossil Record." *Geology* 48: 862–866.
- Moore, K., T. Present, M. Guizar-Sicairos, and M. Holler. 2025. *Data for 'Cretaceous Chert-Hosted Microfossils Visualized With Synchrotron Ptychographic X-Ray Computed Tomography (PXCT)'* [Data set]. CaltechDATA. <https://doi.org/10.22002/xybt1-wpg62>.
- Moore, K. R., T. M. Present, F. Pavia, et al. 2022. "Biosignature Preservation Aided by Organic-Cation Interactions in Proterozoic Tidal Environments." *Palaios* 37, no. 9: 486–498. <https://doi.org/10.2110/palo.2022.017>.
- Moreira, J. L. P., C. V. Madeira, J. A. Gil, and M. A. P. Machado. 2007. "Bacia de Santos." *Boletim Geociencias Petrobras* 12: 531–549.
- Nabhan, S., L. C. Kah, B. Mishra, K. Pollok, A. R. Manning-Berg, and M. A. van Zuilen. 2021. "Structural and Chemical Heterogeneity of Proterozoic Organic Microfossils of the Ca. 1 Ga Old Angmaat Formation, Baffin Island, Canada." *Geobiology* 19, no. 6: 557–584. <https://doi.org/10.1111/gbi.12463>.
- Nakano, C. M. F., A. C. C. Pinto, J. L. Marcusso, and K. Minami. 2009. "Pre-Salt Santos Basin—Extended Well Test and Production Pilot in the Tupi Area—The Planning Phase." Presented at the Offshore Technology Conference, Houston, Texas.
- Odstrčil, M., M. Holler, J. Raabe, and M. Guizar-Sicairos. 2019. "Alignment Methods for Nanotomography With Deep Subpixel Accuracy." *Optics Express* 27: 36637–36652.
- Odstrčil, M., M. Lebugle, M. Guizar-Sicairos, C. David, and M. Holler. 2019. "Towards Optimized Illumination for High-Resolution Ptychography." *Optics Express* 27: 14981–14997.
- Oehler, J. H. 1976. "Hydrothermal Crystallization of Silica Gel." *Geological Society of America Bulletin* 87: 1143.
- Okiongbo, K. S., A. C. Aplin, and S. R. Larter. 2005. "Changes in Type II Kerogen Density as a Function of Maturity: Evidence From the Kimmeridge Clay Formation." *Energy & Fuels* 19: 2495–2499.
- Orange, F., F. Westall, J.-R. Disnar, et al. 2009. "Experimental Silicification of the Extremophilic Archaea *Pyrococcus Abyssii* and *Methanocaldococcus jannaschii*: Applications in the Search for Evidence of Life in Early Earth and Extraterrestrial Rocks." *Geobiology* 7: 403–418.
- Pedersen, E. B. L., D. Angmo, H. F. Dam, et al. 2015. "Improving Organic Tandem Solar Cells Based on Water-Processed Nanoparticles by Quantitative 3D Nanoimaging." *Nanoscale* 7: 13765–13774.
- Phoenix, V. R., D. G. Adams, and K. O. Konhauser. 2000. "Cyanobacterial Viability During Hydrothermal Biomineralisation." *Chemical Geology* 169: 329–338.
- Pietzsch, R., D. M. Oliveira, L. R. Tedeschi, et al. 2018. "Palaeohydrology of the Lower Cretaceous Pre-Salt Lacustrine System, From Rift to Post-Rift Phase, Santos Basin, Brazil." *Palaeogeography, Palaeoclimatology, Palaeoecology* 507: 60–80. <https://doi.org/10.1016/j.palaeo.2018.06.043>.
- Pietzsch, R., L. R. Tedeschi, D. M. Oliveira, C. W. D. dos Anjos, J. C. Vazquez, and M. F. Figueiredo. 2020. "Environmental Conditions of Deposition of the Lower Cretaceous Lacustrine Carbonates of the Barra Velha Formation, Santos Basin (Brazil), Based on Stable Carbon and Oxygen Isotopes: A Continental Record of pCO₂ During the Onset of the Oceanic Anoxic Event 1a (OAE 1a) Interval?" *Chemical Geology* 535: 1–23.
- Rice, C. M., N. H. Trewin, and L. I. Anderson. 2002. "Geological Setting of the Early Devonian Rhynie Cherts, Aberdeenshire, Scotland: An Early Terrestrial Hot Spring System." *Journal of the Geological Society* 159: 203–214.
- Saminpanya, S., and F. L. Sutherland. 2013. "Silica Phase-Transformations During Diagenesis Within Petrified Woods Found in Fluvial Deposits From Thailand–Myanmar." *Sedimentary Geology* 290: 15–26.
- Sauro, F., M. Cappelletti, D. Ghezzi, et al. 2018. "Microbial Diversity and Biosignatures of Amorphous Silica Deposits in Orthoquartzite Caves." *Scientific Reports* 8: 17569.
- Schopf, J. W., and C. Klein. 1992. *The Proterozoic Biosphere: A Multidisciplinary Study*. Cambridge University Press.
- Schultze-Lam, S., F. G. Ferris, K. O. Konhauser, and R. G. Wiese. 1995. "In Situ Silicification of an Icelandic Hot Spring Microbial Mat: Implications for Microfossil Formation." *Canadian Journal of Earth Sciences* 32: 2021–2026.
- Sergeev, V. N., and M. Sharma. 2012. "Proterozoic Fossil Cyanobacteria." *Palaeobotanist* 61: 189–358.
- Siever, R. 1992. "The Silica Cycle in the Precambrian." *Geochimica et Cosmochimica Acta* 56: 3265–3272.
- Slagter, S., W. Hao, N. J. Planavsky, K. O. Konhauser, and L. G. Tarhan. 2022. "Biofilms as Agents of Ediacara-Style Fossilization." *Scientific Reports* 12: 8631.
- Slagter, S., M. Reich, C. Munoz-Saez, et al. 2019. "Environmental Controls on Silica Sinter Formation Revealed by Radiocarbon Dating." *Geology* 47: 330–334.
- Slagter, S., L. G. Tarhan, W. Hao, N. J. Planavsky, and K. O. Konhauser. 2021. "Experimental Evidence Supports Early Silica Cementation of the Ediacara Biota." *Geology* 49: 51–55.
- Stout, L. M., S. R. Joshi, T. M. Kana, and D. P. Jaisi. 2014. "Microbial Activities and Phosphorus Cycling: An Application of Oxygen Isotope Ratios in Phosphate." *Geochimica et Cosmochimica Acta* 138: 101–116.
- Strullu-Derrien, C., P. Kenrick, and A. H. Knoll. 2019. "The Rhynie Chert." *Current Biology* 29: R1218–R1223.
- Suchý, V., L. Borecká, K. Pachnerová Brabcová, et al. 2021. "Microbial Signatures From Speleothems: A Petrographic and Scanning Electron Microscopy Study of Coralloids From the Koněprusy Caves (The Bohemian Karst, Czech Republic)." *Sedimentology* 68: 1198–1226.
- Thibault, P., and M. Guizar-Sicairos. 2012. "Maximum-Likelihood Refinement for Coherent Diffractive Imaging." *New Journal of Physics* 14: 63004.
- Toporski, J. K. W., A. Steele, F. Westall, K. L. Thomas-Keptra, and D. S. McKay. 2002. "The Simulated Silicification of Bacteria—New Clues to the Modes and Timing of Bacterial Preservation and Implications for the Search for Extraterrestrial Microfossils." *Astrobiology* 2: 1–26.

- Tréguer, P., D. M. Nelson, A. J. Van Bennekom, D. J. DeMaster, A. Leynaert, and B. Quéguiner. 1995. "The Silica Balance in the World Ocean: A Reestimate." *Science* 268, no. 5209: 375–379. <https://doi.org/10.1126/science.268.5209.375>.
- Urrutia, M. M., and T. J. Beveridge. 1993. "Remobilization of Heavy Metals Retained as Oxyhydroxides or Silicates by *Bacillus subtilis* Cells." *Applied and Environmental Microbiology* 59: 4323–4329.
- Urrutia, M. M., and T. J. Beveridge. 1994. "Formation of Fine-Grained Metal and Silicate Precipitates on a Bacterial Surface (*Bacillus subtilis*)." *Chemical Geology* 116: 261–280.
- van Heel, M., and M. Schatz. 2005. "Fourier Shell Correlation Threshold Criteria." *Journal of Structural Biology* 151, no. 3: 250–262. <https://doi.org/10.1016/j.jsb.2005.05.009>.
- Vandenbroucke, M., and C. Largeau. 2007. "Kerogen Origin, Evolution and Structure." *Organic Geochemistry* 38: 719–833.
- Wakonig, K., H.-C. Stadler, M. Odstrčil, et al. 2020. "PtychoShelves, a Versatile High-Level Framework for High-Performance Analysis of Ptychographic Data." *Journal of Applied Crystallography* 53: 574–586.
- Walter, M. R., J. Bauld, and T. D. Brock. 1972. "Siliceous Algal and Bacterial Stromatolites in Hot Spring and Geyser Effluents of Yellowstone National Park." *Science* 178: 402–405.
- Westall, F. 1995. "The Experimental Silicification of Microorganisms." *Palaeontology* 38: 495–528.
- Wilmeth, D. T., K. D. Myers, S. V. Lalonde, et al. 2021. "Evaporative Silicification in Floating Microbial Mats: Patterns of Oxygen Production and Preservation Potential in Silica-Undersaturated Streams, El Tatio, Chile." *Geobiology* 20: 1–21.
- Wood, H., A. Barnett, E. Follows, et al. 2024. "The Importance of Core for Carbonate Reservoir Evaluation: A Case Study From the Barra Velha Formation, Santos Basin, Brazil." *Geological Society, London, Special Publications* 548: 159.
- Wright, V. P. 2012. "Lacustrine Carbonates in Rift Settings: The Interaction of Volcanic and Microbial Processes on Carbonate Deposition." *Geological Society, London, Special Publications* 370: 39–47.
- Wright, V. P. 2020. "The Mantle, CO₂ and the Giant Aptian Chemogenic Lacustrine Carbonate Factory of the South Atlantic: Some Carbonates Are Made, Not Born." *Sedimentology* 69: 47–73.
- Wright, V. P., and A. J. Barnett. 2015. "An Abiotic Model for the Development of Textures in Some South Atlantic Early Cretaceous Lacustrine Carbonates." *Geological Society, London, Special Publications* 418: 209–219.
- Yee, N., V. R. Phoenix, K. O. Konhauser, L. G. Benning, and F. G. Ferris. 2003. "The Effect of Cyanobacteria on Silica Precipitation at Neutral pH: Implications for Bacterial Silicification in Geothermal Hot Springs." *Chemical Geology* 199: 83–90.

Supporting Information

Additional supporting information can be found online in the Supporting Information section.